



Supplementary Materials for

Molecular mechanism of biased signaling in a prototypical G protein–coupled receptor

Carl-Mikael Suomivuori, Naomi R. Latorraca, Laura M. Wingler, Stephan Eismann, Matthew C. King, Alissa L. W. Kleinhenz, Meredith A. Skiba, Dean P. Staus, Andrew C. Kruse, Robert J. Lefkowitz, Ron O. Dror

Correspondence to: ron.dror@stanford.edu

This PDF file includes:

Materials and Methods

Figs. S1 to S10

Tables S1 to S2

Description of Auxiliary Supplementary Material

Full Reference List

Materials and methods

System setup for MD simulations

We performed simulations of AT₁R bound to the endogenous, balanced full agonist AngII, to the arrestin-biased ligands TRV023, TRV026, TRV027, and TRV034, to the G-protein-biased ligands TRV055 and TRV056, and to the high-affinity partial agonist S118. We initiated these simulations from the previously published S118-bound AT₁R structure (PDB ID: 6DO1) (20). As a control, we also initiated simulations from the AngII-bound, TRV023-bound, and TRV026-bound structures reported in the companion paper (19). For all simulations, we removed the co-crystallized nanobody from the structures. We modeled the different ligands into the crystal structures by *in silico* mutation using Maestro (Schrödinger) of residues of S118 (for all simulations initiated from the S118-bound structure) or of AngII to match those of each peptide agonist. For TRV026 and TRV055, which contain deletions relative to AngII/S118, we simply deleted the relevant residues. For TRV056, which contains an insertion, we modeled the two N-terminal residues that are shifted by the insertion so that they extended into the extracellular solvent. The designed ligand Ind8-AngII was modeled by adding a connecting methylene group to F8 of AngII (Fig. 5A) in Maestro. For each simulation condition, we performed multiple independent simulations in which initial atom velocities were assigned randomly and independently. In addition to these ligand-bound simulation conditions, we also performed simulations with no ligand present from the S118-bound structure. All simulations are summarized in Table S1.

Missing amino acid side chains and loops were modeled using Prime (Schrödinger) (44, 45). Neutral acetyl and methylamide groups were added to cap the N- and C-termini, respectively, of the protein chains. Titratable residues were kept in their dominant protonation state at pH 7, except for D2.50 (D74), which was protonated (neutral) in all simulations, and D3.49 (D125), which was protonated in the majority of the simulations, as studies indicate that these conserved residues are protonated in active-state GPCRs (46, 47). As D3.49 is close to positively charged groups (*i.e.*, R3.50 and the ICL2 residue R34.54 (R137)) in the nanobody-bound crystal structures (19, 20), we also performed simulations with D3.49 charged. D3.49 was charged in simulations A1–A6, A13–A15, A22–A27, A34–A36, A43–A45, A52–A54, A61–A63, A70–A72, and A79–A81, as well as in the intracellularly restrained simulations B1–B50 (Table S1). D3.49 was neutral in all other simulations. We obtained similar results with D3.49 neutral or charged. Histidine residues were modeled as neutral, with a hydrogen atom bound to either the delta or epsilon nitrogen depending on which tautomeric state optimized the local hydrogen-bonding network. Dowser was used to add water molecules to protein cavities, and the protein structures were aligned on transmembrane (TM) helices 1–4 of the inactive AT₁R crystal structure (PDB ID: 4YAY) (24) in the Orientation of Proteins in Membranes (OPM) database (48). The aligned structures were inserted into a pre-equilibrated palmitoyl-oleoyl-phosphatidylcholine (POPC) membrane bilayer using Dabble (49). Sodium and chloride ions were added to neutralize each system at a concentration of 150 mM. The final systems comprised ~62,000 atoms, including ~130 lipid molecules and ~13,000 water molecules. Approximate system dimensions were 80 Å x 80 Å x 100 Å.

In addition to the AT₁R simulations, we also performed simulations of rhodopsin–arrestin-1 (Table S1, Fig. S4). These simulations, initiated from the rhodopsin–arrestin-1 crystal structure (11), were set up and simulated as described for simulations 15–20 in Supplementary Table 1 of ref. (50) except with Y6.40

(Y257) reverted to methionine and Q3.28 (Q113) reverted to glutamic acid to match the wild-type residues at these positions. In the rhodopsin simulations, D2.50 (D83), E3.37 (E122) and E3.49 (E134) were protonated, in accordance with evidence that these residues are protonated in the active state (51, 52). The prepared protein structures were aligned on the TM helices of the OPM entry for the rhodopsin–arrestin-1 crystal structure (PDB ID: 4ZWJ) (10).

Simulation protocols

The systems were first heated over 12.5 ps from 0 K to 100 K in the NVT ensemble using a Langevin thermostat with harmonic restraints of $10.0 \text{ kcal}\cdot\text{mol}^{-1}\cdot\text{\AA}^{-2}$ on the non-hydrogen atoms of the lipids, protein, and ligand. Initial velocities were sampled from a Boltzmann distribution. The systems were then heated to 310 K over 125 ps in the NPT ensemble. Equilibration was performed at 310 K and 1 bar in the NPT ensemble, with harmonic restraints on the protein and ligand non-hydrogen atoms tapered off by $1.0 \text{ kcal}\cdot\text{mol}^{-1}\cdot\text{\AA}^{-2}$ starting at $5.0 \text{ kcal}\cdot\text{mol}^{-1}\cdot\text{\AA}^{-2}$ in a stepwise manner every 2 ns for 10 ns, and finally by $0.1 \text{ kcal}\cdot\text{mol}^{-1}\cdot\text{\AA}^{-2}$ every 2 ns for an additional 18 ns. Except for intracellularly restrained simulations (see below), all restraints were completely removed during production simulation. Production simulations were performed at 310 K and 1 bar in the NPT ensemble using the Langevin thermostat and Monte Carlo barostat. The simulations were performed using a timestep of 4.0 fs while employing hydrogen mass repartitioning (53). Bond lengths were constrained using SHAKE (54). Non-bonded interactions were cut off at 9.0 Å, and long-range electrostatic interactions were calculated using the particle-mesh Ewald (PME) method with an Ewald coefficient (β) of approximately 0.31 Å and B-spline interpolation of order 4. The PME grid size was chosen such that the width of a grid cell was approximately 1 Å.

We employed the CHARMM36m force field for protein molecules, the CHARMM36 parameter set for lipid molecules and salt ions, and the associated CHARMM TIP3P model for water (55-57). For the rhodopsin–arrestin-1 simulations, we employed the CHARMM36 protein force field (58, 59) rather than the CHARMM36m protein force field, as these simulations were run some years earlier than the current AT₁R simulations.

The AT₁R simulations were performed using the Compute Unified Device Architecture (CUDA) version of particle-mesh Ewald molecular dynamics (PMEMD) in Amber17 (60-62) on graphics processing units (GPUs), apart from the replica-exchange MD simulations described below, which used Amber18 (63) on GPUs. The rhodopsin–arrestin-1 simulations were performed using Amber15 (64) and Amber16 (65). Trajectory snapshots were saved every 200 ps.

In addition to the unbiased simulations in which no artificial forces were present during production simulation, we also performed simulations in which the intracellular portion of the receptor was restrained in its crystallographic nanobody-bound conformation (Table S1). These simulations followed the same protocol as outlined above, but $0.5 \text{ kcal}\cdot\text{mol}^{-1}\cdot\text{\AA}^{-2}$ restraints were applied throughout the production simulation on non-hydrogen atoms of receptor residues that are within 5 Å of the nanobody in the S118-bound crystal structure.

To obtain better sampling of the conformational landscape, we also performed replica-exchange MD (REMD) (66) simulations of AT₁R with each ligand bound, using the S118-bound crystal structure as a

starting point (20). REMD simulation involves a set of coupled simulations (known as replicas) performed at various temperatures, where the higher-temperature simulations serve to accelerate exploration of conformational space by facilitating crossing of energy barriers. For each ligand, we used 36 replicas with temperatures ranging from 310 K to 367.44 K. The set of 36 temperatures was obtained by employing the <http://folding.bmc.uu.se/remd/> web server (67). The temperatures used were the following (in Kelvin): 310.00, 311.53, 313.07, 314.62, 316.17, 317.73, 319.29, 320.86, 322.43, 324.01, 325.60, 327.20, 328.80, 330.40, 332.02, 333.64, 335.26, 336.90, 338.54, 340.19, 341.84, 343.50, 345.16, 346.84, 348.52, 350.20, 351.90, 353.60, 355.30, 357.01, 358.73, 360.46, 362.20, 363.94, 365.69, 367.44. Exchange between neighboring replicas was attempted every 0.4 ps of simulation. We verified that exchange probabilities remained around 30%. The systems were first equilibrated in the NPT ensemble following the protocol described above, after which an additional 10 ns of equilibration was performed in the NVT ensemble. The REMD simulations were performed in the NVT ensemble. Each replica was 3.6 μ s in length. For the analysis of the REMD simulations, we only considered simulation segments performed at 310 K. The REMD simulations were performed on Summit at Oak Ridge National Laboratory. All other simulations were performed on the Sherlock computing cluster at Stanford University.

Simulation analysis protocols

The AmberTools17 CPPTRAJ package (68) was used to reimage trajectories, while Visual Molecular Dynamics (VMD) (69) was used for visualization and analysis.

For Fig. S2, we analyzed representative class-A GPCR structures. Each structure is classified as inactive, active, or intermediate in GPCRdb (70). For clarity, we only picked one active or intermediate structure for a given receptor from each published study (for example, out of PDB entries 4MQS and 4MQT, we picked 4MQS). We picked only one inactive structure per receptor due to the large number of inactive GPCR structures. For the A_{2A} adenosine receptor (A_{2A}AR), we excluded structures with thermostabilizing mutations, as these mutations appear to affect the polar network surrounding N1.50, a key residue involved in stabilizing TM7 in both its alternative and canonical active conformations. We thus plotted data for A_{2A}AR structures corresponding to PDB entries 3QAK (with TM7 alternative), 3EML (with TM7 inactive), 5G53 (with TM7 canonical active), and 6GDG (with TM7 canonical active). AT₁R MD averages were taken over portions of simulations that exhibited stable behavior in either the alternative or canonical active conformations. For the alternative conformation average, we used simulation D36, from 1.5–5.0 μ s. For the canonical active conformation average, we used simulation D35, from 4.0–5.0 μ s.

The structural models in Fig. 2 were prepared by aligning the receptor in MD snapshots of the alternative and canonical active AT₁R conformations to all receptor atoms in G-protein-bound and arrestin-bound GPCR structures using the *align* command in PyMOL. When preparing these models, we only modeled transducer regions that insert into the intracellular side of the receptor—the α 5 helix of Gq and the finger loop of β -arrestin 1. The Gq-bound AT₁R models were prepared based on the structure of the M1 muscarinic acetylcholine receptor (M₁AChR) bound to G11 (9), as the α 5 helix is identical in G11 and Gq. The β -arrestin-1-bound models were prepared based on the rhodopsin–arrestin-1 structure (10), as it was the only available structure of an arrestin bound to a full GPCR. The modeled portion of the arrestin finger loop exhibits high sequence similarity between arrestin-1 and β -arrestins, with two differing positions (β -arrestins 1 and 2 have a leucine at the position corresponding to M75 in arrestin-1; β -arrestin 1 has a

threonine at the position corresponding to S78 in arrestin-1, which is also a serine in β -arrestin 2). The receptor-bound β -arrestin 1 finger loop was modeled by mutating *in silico* (using Maestro) residues of the arrestin-1 finger loop in the rhodopsin–arrestin-1 structure to match those of β -arrestin 1. As the modeled portions of the β -arrestin 1 and β -arrestin 2 finger loops only differ at one residue, models in complex with β -arrestin 1 and β -arrestin 2 yielded essentially identical results.

In Fig. 3B and Fig. S5, we report several distances used to track conformational changes involving residues on TMs 2, 3, and 7. For the position of L3.36, we monitored the distance between the centers of mass of the non-hydrogen side-chain atoms of L3.36 and L2.57 (L81); this distance is also shown in Fig. 4B and Fig. S6. L2.57 was chosen as a stable reference point on TM2. For the position of N3.35, we monitored the distance between the N δ atom of N3.35 and the C γ atom of D2.50. For the position of Y7.43, we monitored the distance between the centers of mass of the non-hydrogen side-chain atoms of Y7.43 and L2.57. For the position of F2.53, we monitored the distance between the C γ atom of F2.53 and the center of mass of the non-hydrogen atoms of the L2.57 side chain. Finally, to quantify TM7 backbone position above the proline kink, we monitored the distance of the side-chain nitrogen of N1.50 to the backbone oxygen of either C7.47 or N7.46. The same distance metrics are shown in Fig. S5. In Fig. S5, we also show the root-mean-square deviation (RMSD) of transmembrane helix backbone atoms in each simulation frame to the initial AT₁R conformation (from the S118-bound crystal structure) after aligning every simulation frame on TMs 1–4 (residues 25–56, 61–90, 97–132 and 141–167). We calculated the RMSD of every non-hydrogen backbone atom for residues 25–56, 61–90, 97–132, 141–167, 193–228, 236–268, and 274–303.

In Fig. 3C, we report an analysis of REMD simulations. For this analysis, we discarded the first 2 μ s to analyze the most equilibrated parts of the simulations. Simulation frames were considered to be in the alternative TM7 conformation if the P7.50–L2.46 distance (measured between the C α atoms) was below 7.0 Å and the χ 1 dihedral angle of Y7.53 was below –150 degrees. To determine whether differences between simulations performed with AngII and those performed with arrestin-biased ligands or G-protein-biased ligands were statistically significant, we performed two-sided *t*-tests of unequal variance (Welch's *t*-tests) on the fraction of time spent in the alternative TM7 conformation, using each REMD simulation as an independent sample. We performed a similar *t*-test to compare simulations with arrestin-biased ligands to simulations with G-protein-biased ligands. We performed and analyzed two independent REMD simulations of AT₁R bound to AngII to increase sampling for this ligand condition. Thus, for the arrestin-biased ligands, *n* = 4; for AngII, *n* = 2; and for Gq-biased ligands, *n* = 2.

All analyses shown in Fig. 4 are based on intracellularly restrained simulations (Table S1), *i.e.*, simulations in which nanobody-contacting residues are gently restrained to their crystallographic positions such that the receptor retains an active intracellular conformation in simulation. In Fig. 4B, the “fraction of time L3.36 in TM2-proximal position” refers to the fraction of simulation frames in which the L3.36–L2.57 distance was below 11.5 Å. To analyze the conformation of peptide residue F8 in Figs. 4B, S6, and S7, we calculated the RMSD of the backbone C atom and the side-chain C β , C γ , and C ζ atoms of F8 to the AngII-bound crystal structure after aligning on the backbone C α and N atoms of peptide residues 7 and 8. To determine whether arrestin-biased ligands and G-protein-biased ligands stabilized significantly different positions of L3.36, we performed a two-sided *t*-test of unequal variance on the fractions of time spent with L3.36 in the TM2-proximal position (as defined above), using 20 simulations of arrestin-biased ligands and 10 simulations of G-protein-biased ligands (5 simulations for each individual ligand). For the analyses in

Fig. 4B, we discarded the first 0.2 μ s of each simulation to achieve better equilibration. The Fig. 4C box plots show the 25th, 50th and 75th percentiles of each distribution for five restrained simulations per ligand (B6–40). Each distribution aggregates the last 1 μ s of each of the 5 simulations per condition. The reported distance is between the Ca atoms of residues D6.58 and R4.64 (R167). We discarded the first 1 μ s for this analysis to ensure that the peptide had fully relaxed in the binding pocket, and to account for the longer observed timescales of helix relaxation at the extracellular surface. We performed a similar analysis to that described for L3.36 to determine whether G-protein-biased ligands and AngII, as well as G-protein-biased ligands and arrestin-biased ligands, favored significantly different TM6–TM4 extracellular distances, but here we compared mean TM6–TM4 distances, with each simulation representing an independent sample.

In Fig. 5A, we show superimposed frames from every 500 ns of simulation from five independent 2- μ s intracellularly restrained simulations per ligand, initiated from the S118-bound crystal structure. The trajectories were aligned on TMs 1–4 of the receptor in the S118-bound crystal structure.

In Figs. 1, 3B, 4B, S4, S5, and S6, we show both unsmoothed traces (thin lines) and traces smoothed with a moving average (thick lines). We use an averaging window of 20 ns, except for Fig. 4B and Fig. S6, in which we use an averaging window of 10 ns. In Fig. S3, no smoothing is applied.

Radioligand binding

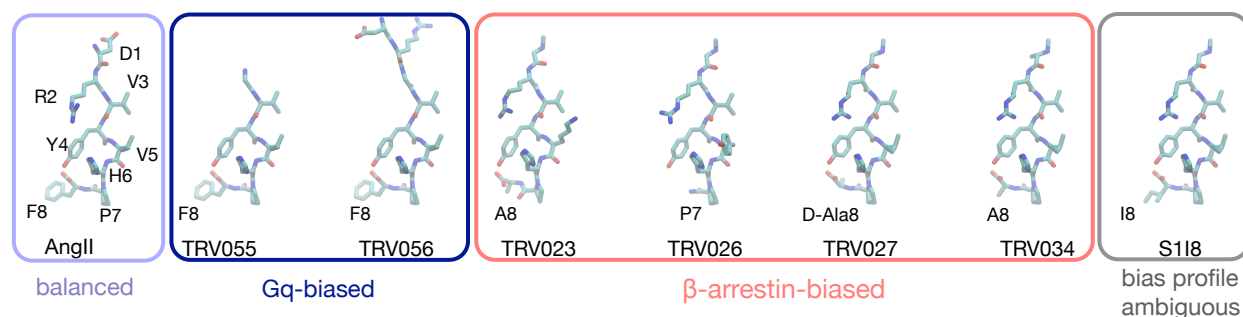
Crude cell membranes were prepared from tetracycline-inducible Expi293F cells (71) transfected with pcDNA-Zeo-tetO-FLAG-human AT₁R (20) as previously described (14). In competition binding experiments, membranes were incubated with varying concentrations of cold competitor ligand and 2.5 nM [³H]-olmesartan (American Radiolabeled Chemicals) in a total volume of 200 μ L and assay buffer comprised of 50 mM Tris pH 7.4, 150 mM NaCl, 12.5 mM MgCl₂, 0.2% bovine serum albumin (BSA), leupeptin, and benzamidine. After a 90-minute incubation at room temperature, reactions were harvested onto GF/B filters and quickly washed three times with cold 50 mM Tris pH 7.4. Data were analyzed in GraphPad Prism using a one-site competition binding model. *K_i* determinations were based on the experimentally determined [³H]-olmesartan affinity for each mutant. Radioligand affinity was determined through a saturation-binding curve with a serial dilution of [³H]-olmesartan, with non-specific binding determined in the presence of 10 μ M candesartan. These data were fit to a one-site saturation-binding model in GraphPad Prism. All radioligand binding reactions were performed in duplicate, and 3–4 independent experiments were performed for each ligand.

Cell-based assays

Gq activity was assayed based on inositol monophosphate (IP1) accumulation as measured using the IP-One Gq Kit (Cisbio). The activities of novel analogs (Fig. 5) were assayed in tetracycline-inducible Expi293F cells stably expressing FLAG-human AT₁R wild-type (20). Twenty thousand cells were seeded into each well of a 96-well low volume plate (Cisbio). Cells were stimulated with ligands at 37 °C for 2 hours, and IP1 was quantified according to the manufacturer protocol using a CLARIOstar plate reader (BMG Labtech). Three to four independent experiments were performed with single replicates. Data from each experiment were normalized by setting non-stimulated wells as 0% and the maximal AngII response

(determined by a sigmoidal dose response curve in GraphPad Prism) as 100%. The combined datasets were fit with a sigmoidal dose response curve in GraphPad Prism.

The PathHunter assay (DiscoverX) was used to monitor translocation of β -arrestin 2 to endosomes as previously described (4). U2OS cells stably expressing β -arrestin 2–Enzyme Acceptor tag and endosome-localized ProLink tag protein were transiently transfected with pcDNA-Zeo-tetO-FLAG-human AT₁R wild-type. One day post-transfection, 35,000 cells were plated in each well of a 96-well plate. Two days post-transfection, the plated cells were treated with ligands for 3 hours at 37 °C. β -Galactosidase activity was detected following the manufacturer's protocol using a CLARIOstar plate reader (BMG Labtech). Three independent experiments were performed with single replicates, and data were normalized to 100% of the maximal AngII response using a sigmoidal dose response curve fit in GraphPad Prism.



ligand	sequence (numbering based on AngII)							
	1	2	3	4	5	6	7	8
AngII	Asp	Arg	Val	Tyr	Ile	His	Pro	Phe
TRV055	Asp	Gly	Val	Tyr	Ile	His	Pro	Phe
TRV056		Arg	Gly	Val	Tyr	Ile	His	Pro
TRV023		Sar	Arg	Val	Tyr	Lys	His	Pro
TRV026		Sar	Arg	Val	Tyr	Tyr	His	Pro
TRV027		Sar	Arg	Val	Tyr	Ile	His	Pro
TRV034		NMe-Ala	Arg	Val	Tyr	Ile	His	Pro
S118		Sar	Arg	Val	Tyr	Ile	His	Pro

Fig. S1. Structures and sequences of simulated AT₁R ligands. Compared to the balanced ligand AngII, the Gq-biased ligands show greater Gq-coupling efficacy but similar arrestin coupling in *in vitro* transducer coupling assays (14). The β -arrestin-biased ligands promote coupling to arrestin but not Gq in *in vitro* transducer coupling assays (14). The bias profile of S118 has not been rigorously analyzed, and S118 has been previously described as an antagonist (72), an arrestin-biased agonist (73), and a partial agonist (74). S118 appears to be somewhat arrestin-biased in the assays used in the companion paper (19). It also appears to be β -arrestin-biased in our simulations: the fraction of time spent in the alternative TM7 conformation in REMD simulations of AT₁R bound to S118 is 0.39, similar to the β -arrestin-biased ligands (Fig. 3C). Sarcosine (Sar) is N-methyl (NMe) glycine.

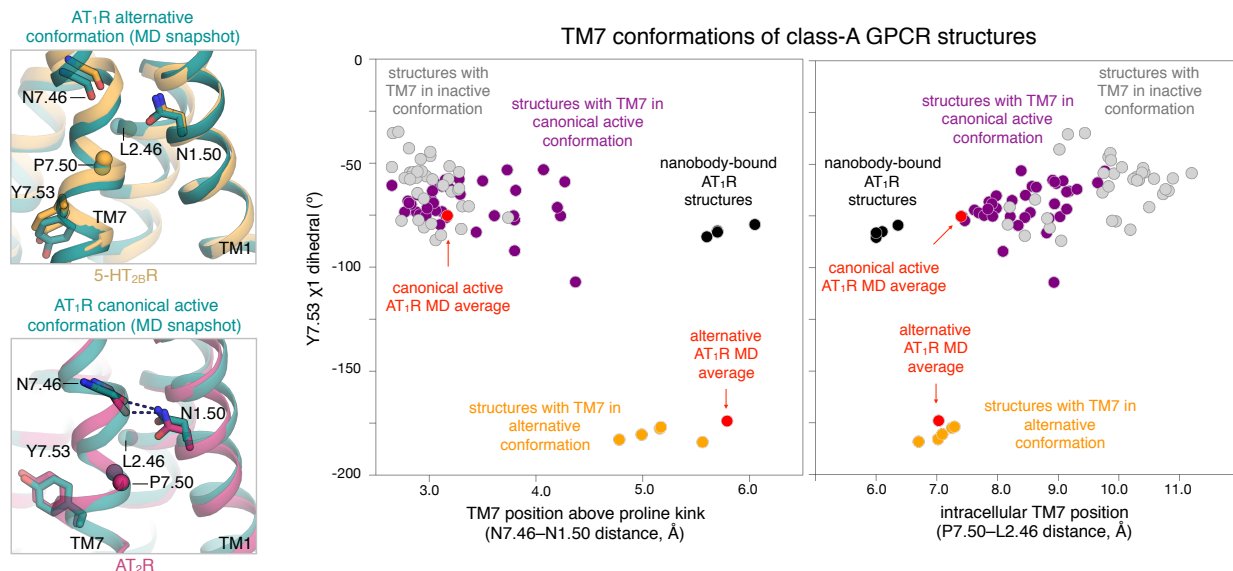


Fig. S2. Observed conformations of TM7 in AT₁R simulations match experimental structures of certain other GPCRs. Left: The alternative TM7 conformation of AT₁R closely resembles the crystal structure of 5-HT_{2B}R bound to the arrestin-biased ligand ergotamine, whereas the canonical active conformation closely resembles the active-state structure of AT₂R. Right: Experimental structures of class-A GPCRs cluster into distinct groups based on TM7 conformation (as characterized by the values plotted in Fig. 1 as well as the P7.50–L2.46 C α –C α distance, which specifies the backbone position of the intracellular portion of TM7). The nanobody-bound AT₁R crystal structures are unusual, but each of the two AT₁R TM7 conformations observed in simulation matches experimental structures of other GPCRs.

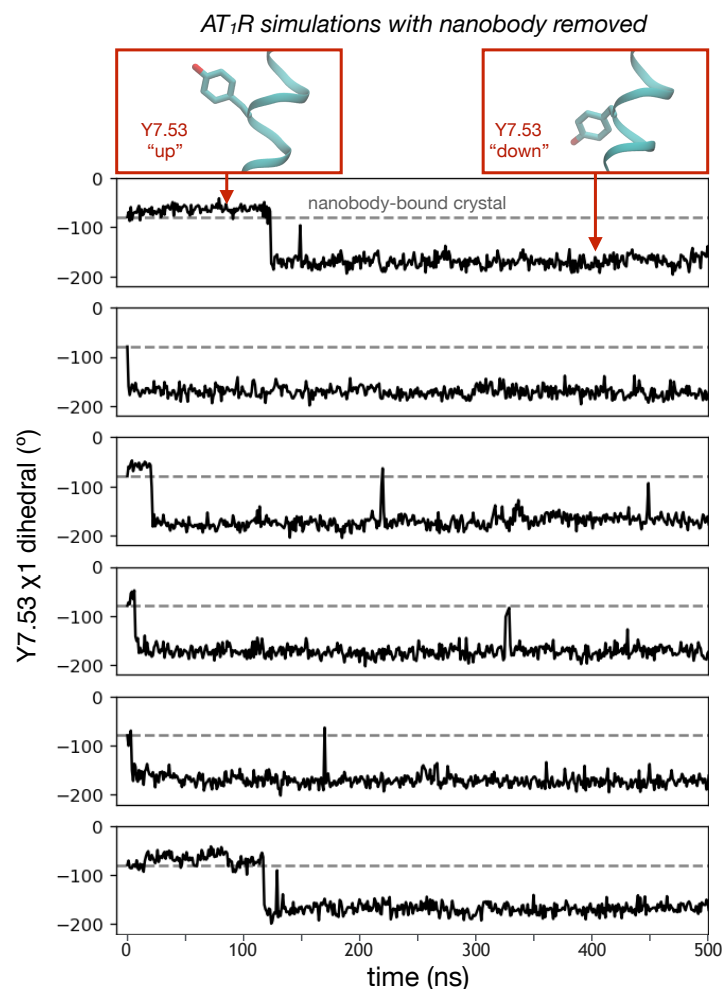


Fig. S3. Upon removal of the nanobody, AT₁R quickly relaxes to the alternative conformation in simulation, with Y7.53 adopting a rotamer that points toward the intracellular side. Shown are traces for the first 500 ns of six simulations of S118-bound AT₁R, initiated from the S118-bound crystal structure but with the nanobody removed. Dashed lines indicate the crystallographic dihedral angle (upward rotamer), whereas values below $\sim -150^\circ$ indicate that Y7.53 has adopted the downward rotamer associated with the alternative conformation.

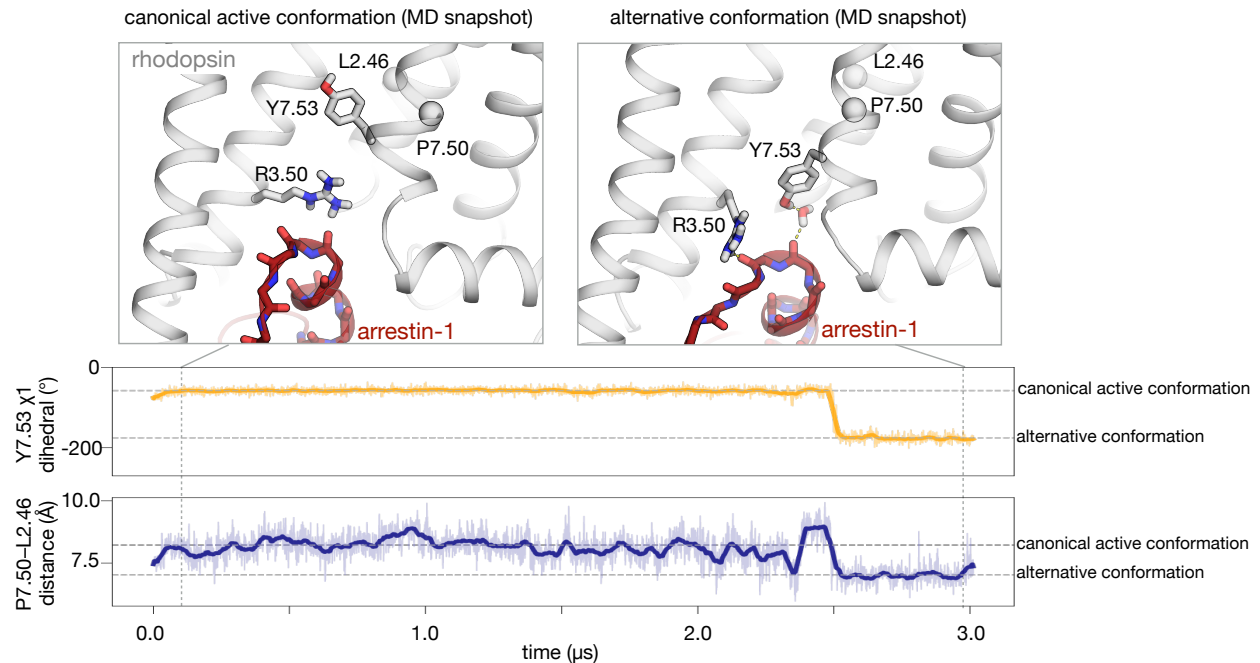


Fig. S4. Arrestin-bound rhodopsin spontaneously transitions between canonical active and alternative conformations in simulation. In simulations of rhodopsin bound to arrestin-1 (visual arrestin), the receptor can spontaneously adopt the alternative conformation, with Y7.53 and R3.50 of rhodopsin forming polar interactions with the arrestin finger loop. Traces are shown for a simulation that transitions to an alternative conformation after about 2.5 μs , with Y7.53 adopting a downward rotamer and the distance between TM7 and TM2 decreasing. Horizontal dashed lines correspond to average values in the canonical active conformation (top line in each plot) and average values in the alternative conformation (bottom line in each plot). Average values were computed over stable parts of this simulation (from 0.5 to 2.0 μs for the canonical active conformation and from 2.5 to 3.0 μs for the alternative conformation).

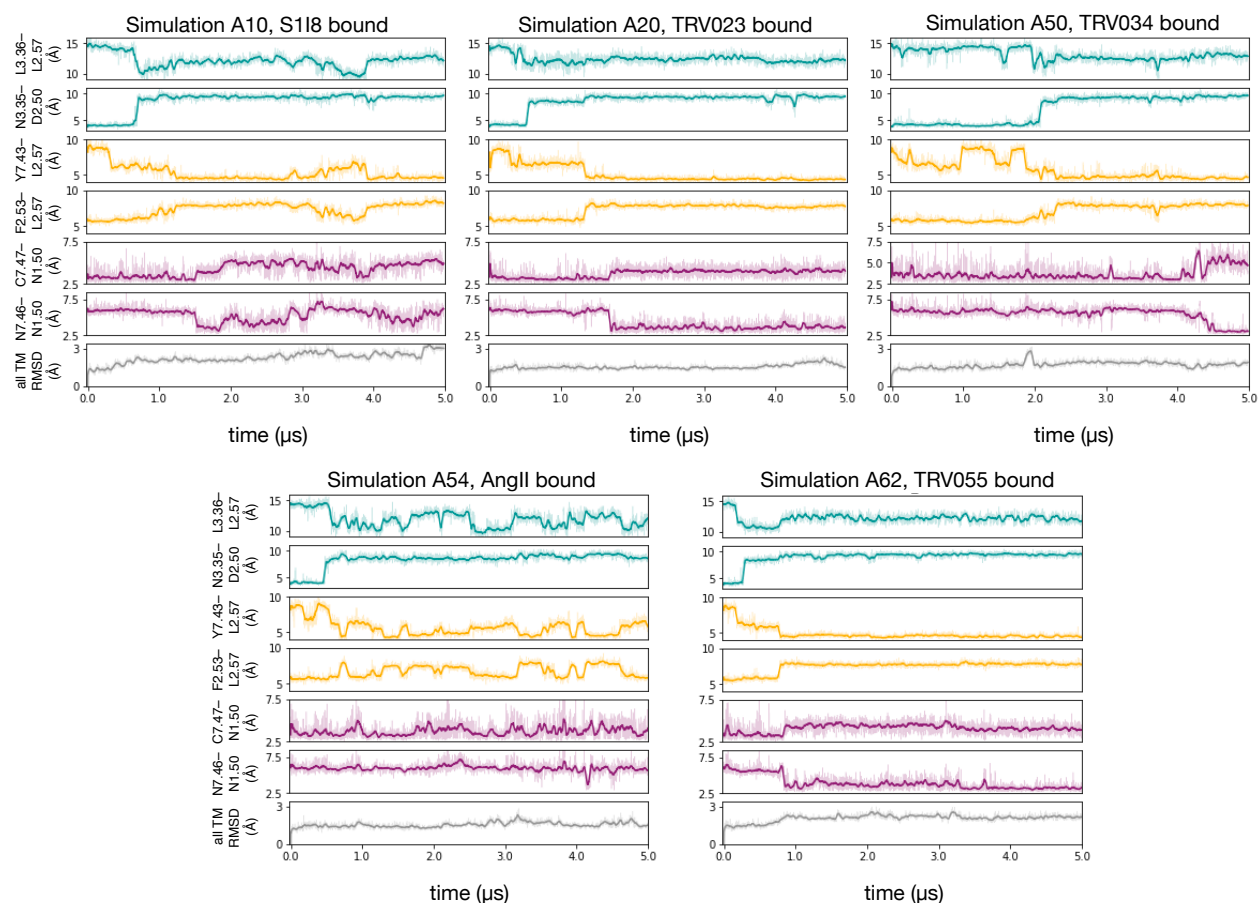


Fig. S5. Allosteric coupling between AT₁R regions linking the ligand-binding pocket to the intracellular side. Traces show the same quantities as in Fig. 3B, as well as the root-mean-square deviation (RMSD) of transmembrane helix backbone atoms to the initial crystal structure (see Methods), for five representative simulations initiated from the S1I8-bound crystal structure. Similar behavior was observed in simulations initiated from the other active-state crystal structures. The simulation numbers are from Table S1.

Simulations of AngII-bound AT₁R

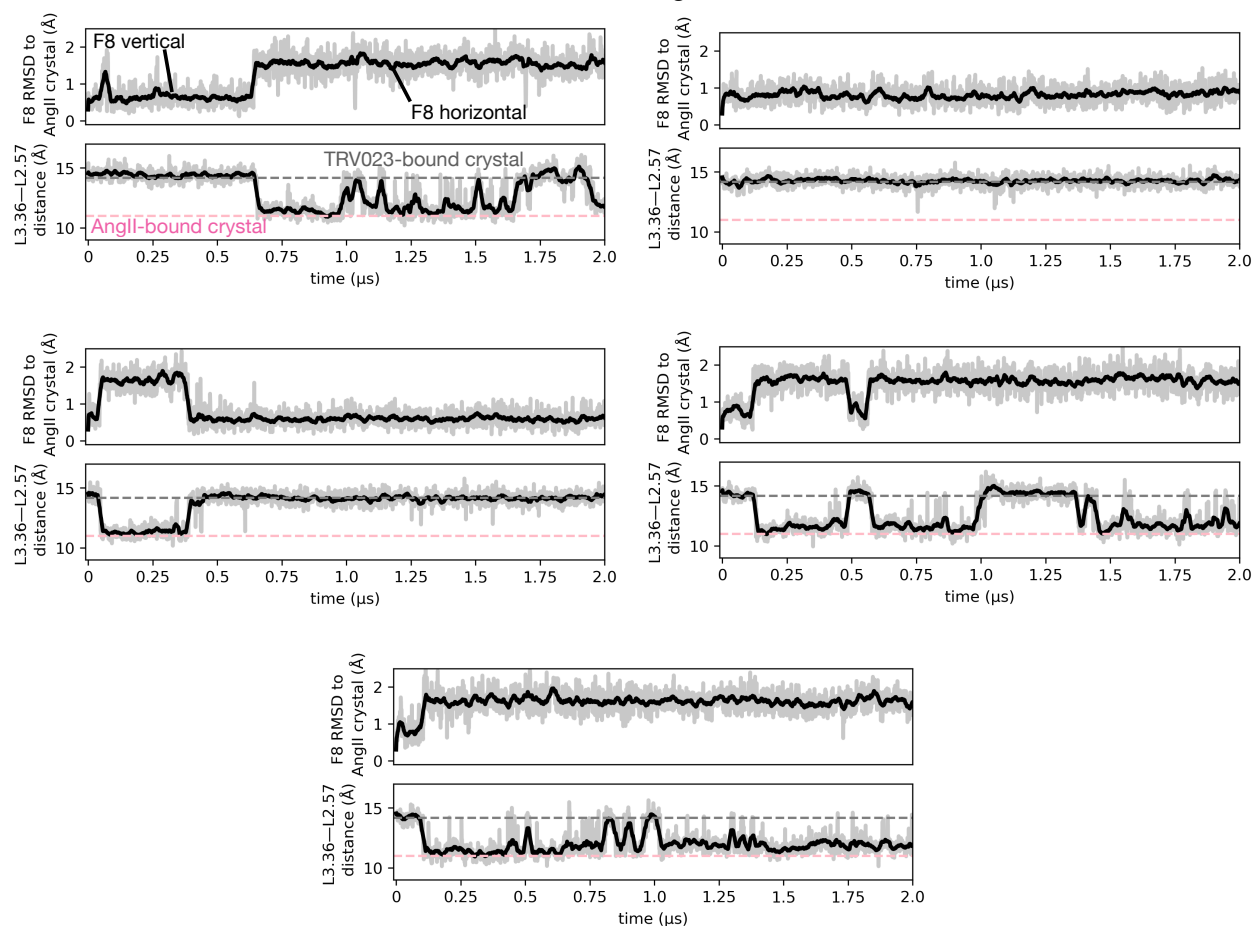


Fig. S6. The position of L3.36 correlates with the orientation of the C-terminal phenyl ring (F8) of AngII. Traces show the same quantities as in Fig. 4B, but for all AngII-bound simulations with the intracellular side of the receptor gently restrained to its crystallographic position (to prevent changes in the global conformational state of the receptor). All of these simulations were initiated from the S118-bound crystal structure, with AngII modeled in.

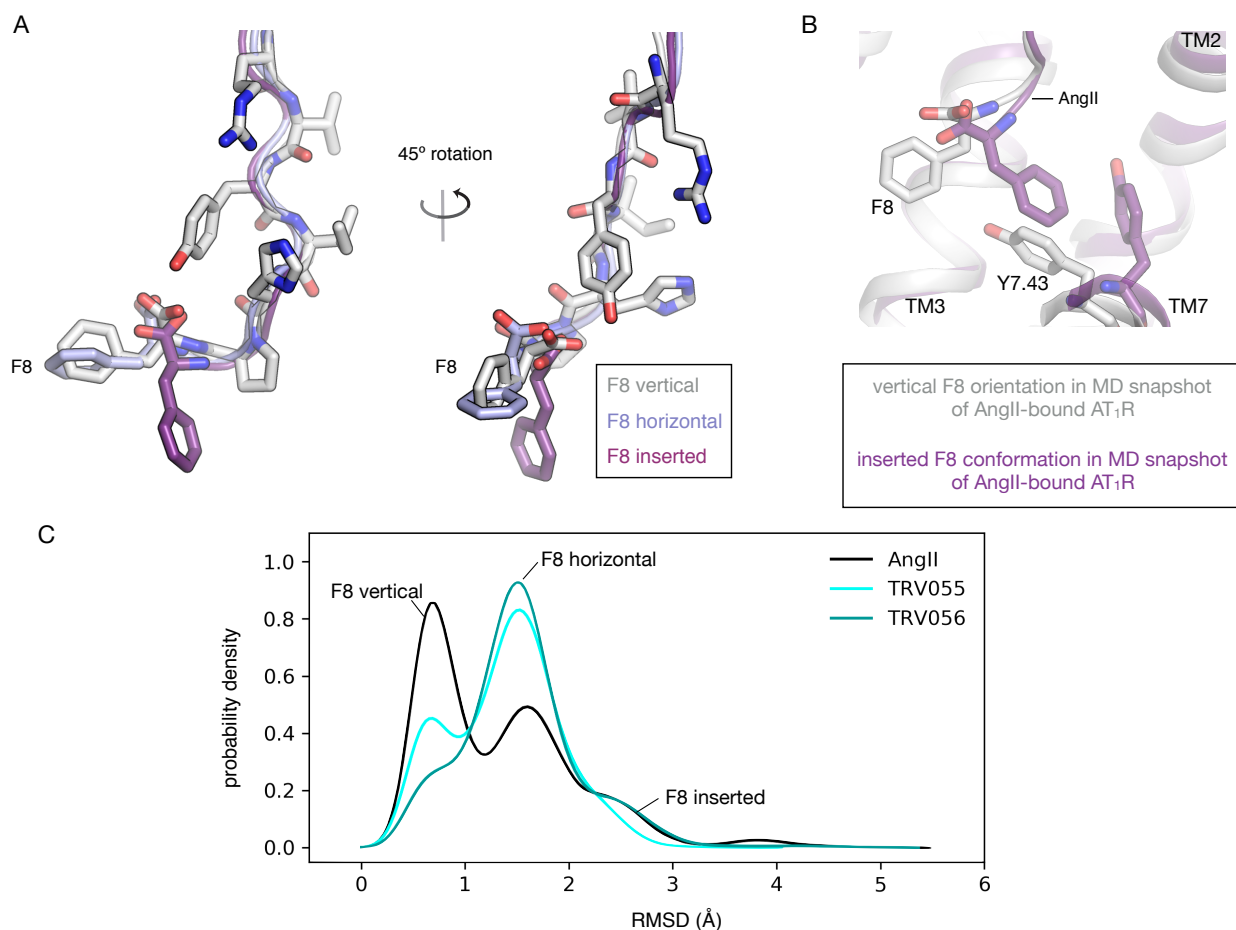


Fig. S7. The C-terminal F8 residue of AngII and G-protein-biased ligands adopts multiple conformations in simulation. (A) Representative snapshots of AngII from AngII-bound AT₁R simulations, showing the two major orientations adopted by the C-terminal F8 residue (the vertical and horizontal orientations), as well as an “inserted” conformation, which F8 occasionally adopts. (B) When F8 adopts the “inserted” conformation, it interacts directly with AT₁R residue Y7.43; this might help AngII and G-protein-biased ligands stabilize the canonical active TM7 conformation. (C) Gq-biased ligands TRV055 and TRV056 were more likely than AngII to adopt the horizontal F8 orientation in simulation. Probability distributions represent aggregated data from nine 5-μs simulations for each ligand.

Simulation of AngII-bound AT₁R, started from S118-bound crystal structure

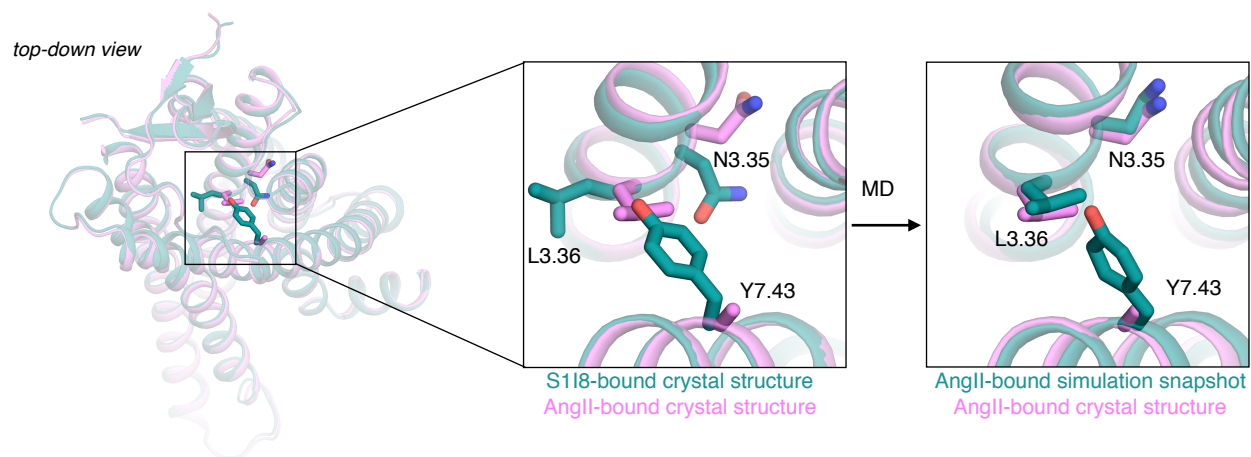


Fig. S8. Simulations initiated from the previously published active-state structure recapitulate conformational changes seen in AngII-bound crystal structure. In simulations initiated from the previously published (S118-bound) crystal structure (20), with the co-crystallized ligand replaced by AngII, the region beneath the binding pocket spontaneously adopts the conformation seen in the AngII-bound crystal structure of the companion paper (19). The side chain of Y7.43 is not resolved in the AngII-bound structure. The TRV023-bound and TRV026-bound structures of the companion paper are essentially identical to the previously published S118-bound structure.

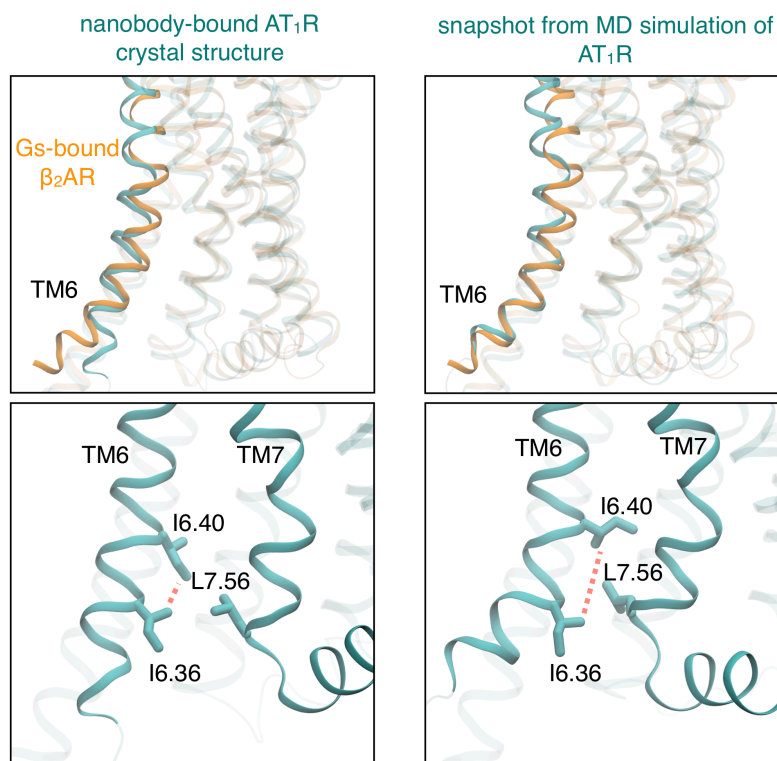


Fig. S9. In simulation, AT₁R occasionally adopts the TM6-bent conformation, which differs from the canonical active conformation in that the intracellular end of TM6 is further from the center of the helical bundle. In a representative simulation snapshot of the TM6-bent AT₁R conformation, the TM6 conformation closely matches that observed in the crystal structure of β_2 AR bound to Gs (top right), whereas the TM6 conformation of nanobody-bound AT₁R crystal structures differs from that in the β_2 AR–Gs structure (top left). When AT₁R adopts the TM6-bent conformation, TM6 bends outward as the side chain of L7.56 inserts between the side chains of I6.40 and I6.36 on TM6 (bottom, left and right). The simulation snapshot shown is from an AngII-bound AT₁R simulation, but AT₁R also adopts this conformation in simulations with other ligands bound.

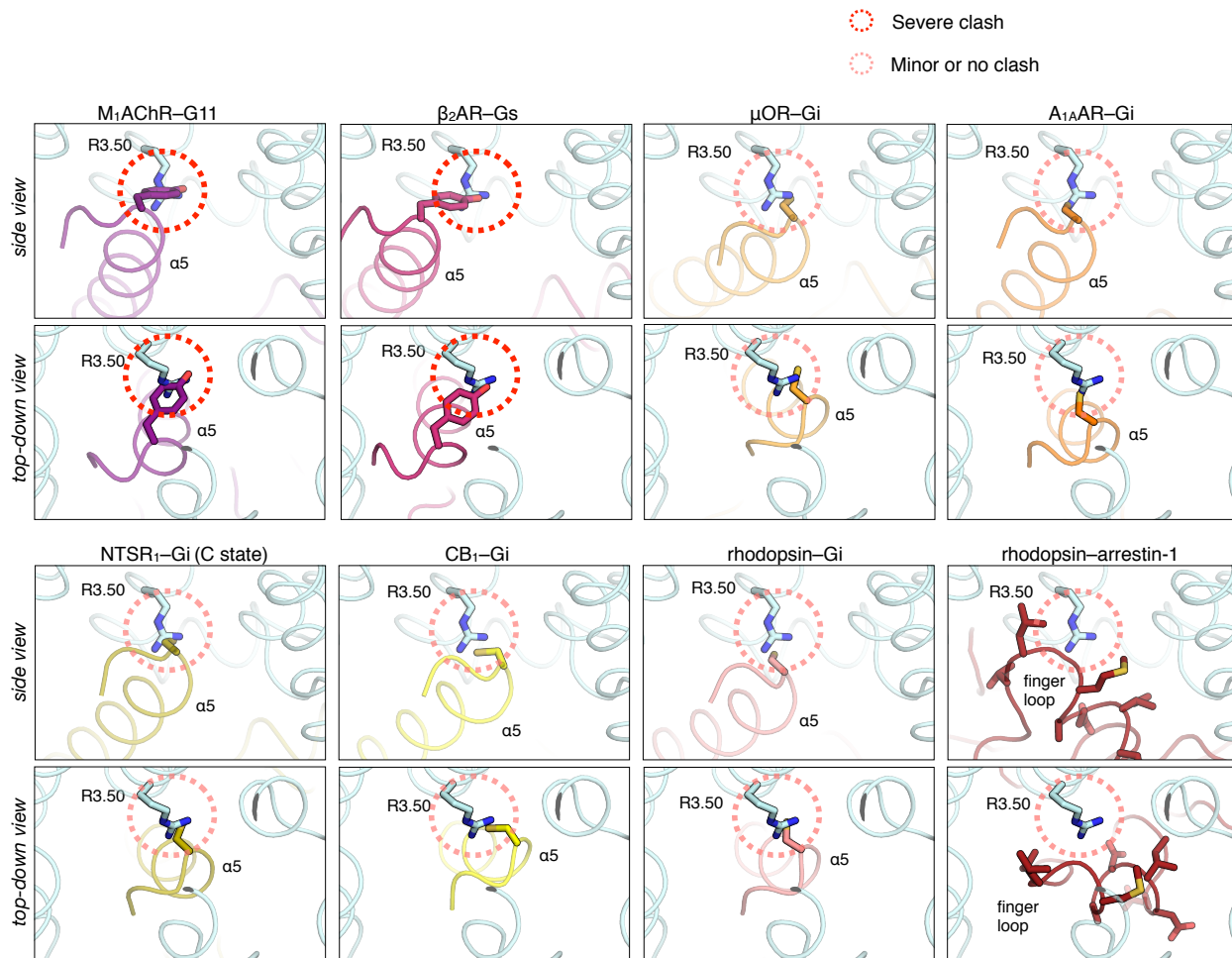


Fig. S10. Steric hindrance between the side chain of R3.50 in a GPCR and the $\alpha 5$ helix in the α subunit of a bound G protein varies with G-protein subtype and orientation. Although the downward R3.50 rotamer of the alternative conformation (cyan) disfavors coupling to G proteins (other colors), certain G-protein subtypes may couple to this receptor conformation in experimentally observed orientations. In particular, Gi/o has a cysteine at the same position as the $\alpha 5$ helix tyrosine that clashes with R3.50 when Gs or Gq/11 are bound, leading to less severe clashing with R3.50. Steric hindrance between the cysteine and R3.50 appears to be further reduced when Gi adopts certain orientations observed in experimental GPCR–Gi structures. The arrestin-1 finger loop (dark red) does not appear to clash with the downward R3.50 rotamer, and the same applies to the finger loop of β -arrestins 1 and 2. The alternative conformation is represented here by the AngII-bound AT₁R crystal structure, which shares the downward R3.50 rotamer as well as TM helix positions as the alternative AT₁R conformation from simulation. In each panel, the AngII-bound AT₁R crystal structure is aligned to the receptor in experimental GPCR–G protein and GPCR–arrestin complexes.

Ligand	Simulation number	Duration (μ s)	Notes
Condition A: AT_IR, from S1I8-bound crystal structure			
S1I8	A1–12	5.0 (each)	A7–A12 shown in Fig. S3. A10 shown in Fig. S5.
TRV023	A13–21	5.0 (each)	A20 shown in Fig. S5.
TRV026	A22–33	5.0 (each)	
TRV027	A34–42	5.0 (each)	
TRV034	A43–51	5.0 (each)	A50 shown in Fig. S5.
AngII	A52–60	5.0 (each)	Shown in Fig. S7. A54 shown in Fig. S5.
TRV055	A61–69	5.0 (each)	Shown in Fig. S7. A62 shown in Fig. 3B, S5.
TRV056	A70–78	5.0 (each)	Shown in Fig. S7.
none	A79–87	5.0 (each)	
Condition B: AT_IR, from S1I8-bound crystal structure, with intracellular restraints			
S1I8	B1–5	2.0 (each)	
TRV023	B6–10	2.0 (each)	Shown in Fig. 4B, 4C.
TRV026	B11–15	2.0 (each)	Shown in Fig. 4B, 4C.
TRV027	B16–20	2.0 (each)	Shown in Fig. 4B, 4C.
TRV034	B21–25	2.0 (each)	Shown in Fig. 4B, 4C.
AngII	B26–30	2.0 (each)	Shown in Fig. 4B, 4C, 5A, S6. Traces in Fig. 4B are from simulation B28.
TRV055	B31–35	2.0 (each)	Shown in Fig. 4B, 4C.
TRV056	B36–40	2.0 (each)	Shown in Fig. 4B, 4C.
Ind8-AngII	B41–45	2.0 (each)	Shown in Fig. 5A.
none	B46–50	2.0 (each)	
Condition C: AT_IR, REMD from S1I8-bound crystal structure			
S1I8	C1	3.6 for each of 36 replicas	
TRV023	C2	3.6 for each of 36 replicas	Shown in Fig. 3C.
TRV026	C3	3.6 for each of 36 replicas	Shown in Fig. 3C.
TRV027	C4	3.6 for each of 36 replicas	Shown in Fig. 3C.
TRV034	C5	3.6 for each of 36 replicas	Shown in Fig. 3C.
AngII	C6	3.6 for each of 36 replicas	Shown in Fig. 3C.
AngII	C7	3.6 for each of 36 replicas	Shown in Fig. 3C.
TRV055	C8	3.6 for each of 36 replicas	Shown in Fig. 3C.
TRV056	C9	3.6 for each of 36 replicas	Shown in Fig. 3C.
Condition D: AT_IR, from AngII-bound crystal structure			
S1I8	D1–6	5.0 (each)	
TRV023	D7–12	5.0 (each)	
TRV026	D13–18	5.0 (each)	
TRV027	D19–24	5.0 (each)	
TRV034	D25–30	5.0 (each)	
AngII	D31–36	5.0 (each)	D35 shown in Fig. 1.
TRV055	D37–42	5.0 (each)	
TRV056	D43–48	5.0 (each)	
Condition E: AT_IR, from TRV023-bound crystal structure			
TRV023	E1–6	5.0 (each)	

Condition F: AT₁R, from TRV026-bound crystal structure			
TRV026	F1–6	5.0 (each)	
Condition G: rhodopsin–arrestin-1			
none	G1–5	3.0 (each)	G5 shown in Fig. S4.

Table S1

Summary of simulations performed in this work. The co-crystallized nanobody was removed before each AT₁R simulation. “Intracellular restraints” indicates that the intracellular portion of the receptor was restrained in the crystallographic, nanobody-bound conformation. For the REMD simulations, the reported length (3.6 μ s) corresponds to the length of each replica. The “notes” column indicates which simulations are shown in traces or analyses in main text or supplemental figures.

Ligand	Binding affinity	Gq activation		β -arrestin activation	
	Log Ki (M)	Log EC50 (M)	E _{max} –baseline	Log EC50 (M)	E _{max} –baseline
AngII	-7.47 ± 0.07	-9.8 ± 0.1	78.5 ± 5.7	-8.5 ± 0.1	99 ± 5
Ind8-AngII	-7.42 ± 0.09	ND	ND	-8.56 ± 0.04	56.3 ± 0.9
S1I8	-8.75 ± 0.02	-8.4 ± 0.3	25.5 ± 3.5	-8.2 ± 0.08	61 ± 2
S1A2I8	-6.66 ± 0.04	-8.2 ± 0.2	39.6 ± 2.7	-7.77 ± 0.04	59 ± 1

Table S2.

Binding affinities and functional measurements for designed ligands and for the ligands from which they were derived. Log Ki values represent the logarithm of the equilibrium dissociation constant and were determined through competition-binding experiments with a radioligand, [³H]-olmesartan. The K_d of [³H]-olmesartan (1.2 ± 0.1 nM) was determined through a saturation-binding experiment (see Methods). Log EC₅₀, baseline, and E_{max} values were determined from sigmoidal dose-response fits of the Gq and β -arrestin activation data shown in Figure 5 (see Methods). E_{max} and baseline values represent percent of maximal AngII response. Gq activation of Ind8-AngII was too low to fit a sigmoidal dose-response curve, so Log EC₅₀ and E_{max}–baseline are listed as ND (not determined) in this case. Error represents standard error determined from 3–4 independent experiments.

Auxiliary supplementary material: representative simulation frames of the alternative and canonical active conformational states of AT₁R.

alternative_conformation_simulation_A10_27ns.pdb. Representative simulation frame of S1I8-bound AT₁R in alternative conformation. The frame is from $t = 27.0$ ns of simulation A10 (Table S1). The receptor is aligned on TMs 1–4 of the S1I8-bound AT₁R crystal structure.

canonical_active_conformation_simulation_A10_1611ns.pdb. Representative simulation frame of S1I8-bound AT₁R in canonical active conformation. The frame is from $t = 1611.0$ ns of simulation A10 (Table S1). The receptor is aligned on TMs 1–4 of the S1I8-bound AT₁R crystal structure.

References and notes:

1. R. Santos *et al.*, A comprehensive map of molecular drug targets. *Nat. Rev. Drug Discov.* **16**, 19–34 (2016).
2. L. Tan, W. Yan, J. D. McCorvy, J. Cheng, Biased Ligands of G Protein-Coupled Receptors (GPCRs): Structure–Functional Selectivity Relationships (SFSRs) and Therapeutic Potential. *J. Med. Chem.* **61**, 9841–9878 (2018).
3. J. J. Liu, R. Horst, V. Katritch, R. C. Stevens, K. Wüthrich, Biased signaling pathways in β_2 -adrenergic receptor characterized by 19F-NMR. *Science* **335**, 1106–1110 (2012).
4. L. M. Wingler *et al.*, Angiotensin analogs with divergent bias stabilize distinct receptor conformations. *Cell* **176**, 468–478. e411 (2019).

5. S. G. Rasmussen *et al.*, Crystal structure of the β_2 adrenergic receptor–Gs protein complex. *Nature* **477**, 549-555 (2011).
6. J. García-Nafria, Y. Lee, X. Bai, B. Carpenter, C. G. Tate, Cryo-EM structure of the adenosine A_{2A} receptor coupled to an engineered heterotrimeric G protein. *Elife* **7**, e35946 (2018).
7. A. Koehl *et al.*, Structure of the μ -opioid receptor–G_i protein complex. *Nature* **558**, 547-552 (2018).
8. A. Glukhova *et al.*, Rules of engagement: GPCRs and G proteins. *ACS Pharmacol. Transl. Sci.* **1**, 73-83 (2018).
9. S. Maeda, Q. Qu, M. J. Robertson, G. Skiniotis, B. K. Kobilka, Structures of the M1 and M2 muscarinic acetylcholine receptor/G-protein complexes. *Science* **364**, 552-557 (2019).
10. Y. Kang *et al.*, Crystal structure of rhodopsin bound to arrestin by femtosecond X-ray laser. *Nature* **523**, 561-567 (2015).
11. X. E. Zhou *et al.*, Identification of phosphorylation codes for arrestin recruitment by G protein-coupled receptors. *Cell* **170**, 457-469. e413 (2017).
12. W. Yin *et al.*, A complex structure of arrestin-2 bound to a G protein-coupled receptor. *Cell Res.* **29**, 971-983 (2019).
13. S. Rajagopal *et al.*, Quantifying ligand bias at seven-transmembrane receptors. *Mol. Pharmacol.* **80**, 367-377 (2011).
14. R. T. Strachan *et al.*, Divergent transducer-specific molecular efficacies generate biased agonism at a G protein-coupled receptor (GPCR). *J. Biol. Chem.* **289**, 14211-14224 (2014).
15. J. Cabana *et al.*, Identification of Distinct Conformations of the Angiotensin-II Type 1 Receptor Associated with the Gq/11 Protein Pathway and the β -Arrestin Pathway Using Molecular Dynamics Simulations. *J. Biol. Chem.* **290**, 15835-158354 (2015).
16. J. D. Violin *et al.*, Selectively engaging β -arrestins at the angiotensin II type 1 receptor reduces blood pressure and increases cardiac performance. *J. Pharmacol. Exp. Ther.* **335**, 572-579 (2010).
17. S. M. DeWire, J. D. Violin, Biased ligands for better cardiovascular drugs: dissecting G-protein-coupled receptor pharmacology. *Circ. Res.* **109**, 205-216 (2011).
18. D. M. Ryba *et al.*, Long-term biased β -arrestin signaling improves cardiac structure and function in dilated cardiomyopathy. *Circulation* **135**, 1056-1070 (2017).
19. L. M. Wingler *et al.*, Angiotensin II and biased analogs induce structurally distinct active conformations within a GPCR. (companion paper).
20. L. M. Wingler, C. McMahon, D. P. Staus, R. J. Lefkowitz, A. C. Kruse, Distinctive activation mechanism for angiotensin receptor revealed by a synthetic nanobody. *Cell* **176**, 479-490. e412 (2019).
21. H. Asada *et al.*, Crystal structure of the human angiotensin II type 2 receptor bound to an angiotensin II analog. *Nat. Struct. Mol. Biol.* **25**, 570-576 (2018).

22. J. A. Ballesteros, H. Weinstein, in *Receptor Molecular Biology*, vol. 25 of *Methods in Neurosciences*, S. C. Sealford, Ed. (Elsevier, 1995), chap. 19, pp. 366-428.
23. W. I. Weis, B. K. Kobilka, The Molecular Basis of G Protein–Coupled Receptor Activation. *Annu. Rev. Biochem.* **87**, 897-919 (2018).
24. H. Zhang *et al.*, Structure of the angiotensin receptor revealed by serial femtosecond crystallography. *Cell* **161**, 833-844 (2015).
25. F. Xu *et al.*, Structure of an Agonist-Bound Human A_{2A} Adenosine Receptor. *Science* **332**, 322-327 (2011).
26. D. Wacker *et al.*, Structural features for functional selectivity at serotonin receptors. *Science* **340**, 615-619 (2013).
27. W. Liu *et al.*, Serial femtosecond crystallography of G protein–coupled receptors. *Science* **342**, 1521-1524 (2013).
28. D. Wacker *et al.*, Crystal structure of an LSD-bound human serotonin receptor. *Cell* **168**, 377-389. e312 (2017).
29. J. D. McCorvy *et al.*, Structural determinants of 5-HT_{2B} receptor activation and biased agonism. *Nature Struct. Mol. Biol.* **25**, 787 (2018).
30. G. Lebon *et al.*, Agonist-bound adenosine A_{2A} receptor structures reveal common features of GPCR activation. *Nature* **474**, 521 (2011).
31. R. O. Dror *et al.*, Activation mechanism of the β_2 -adrenergic receptor. *Proc. Natl. Acad. Sci. U.S.A.* **108**, 18684-18689 (2011).
32. A. J. Venkatakrishnan *et al.*, Diverse activation pathways in class A GPCRs converge near the G-protein-coupling region. *Nature* **536**, 484-487 (2016).
33. N. R. Latorraca, A. Venkatakrishnan, R. O. Dror, GPCR dynamics: structures in motion. *Chem. Rev.* **117**, 139-155 (2017).
34. S. Yuan, S. Filipek, K. Palczewski, H. Vogel, Activation of G-protein-coupled receptors correlates with the formation of a continuous internal water pathway. *Nat. Commun.* **5**, 4733 (2014).
35. B. C. Taylor, C. T. Lee, R. E. Amaro, Structural basis for ligand modulation of the CCR2 conformational landscape. *Proc. Natl. Acad. Sci. U.S.A.* **116**, 8131-8136 (2019).
36. R. Nygaard *et al.*, The dynamic process of β_2 -adrenergic receptor activation. *Cell* **152**, 532-542 (2013).
37. A. Manglik *et al.*, Structure-based discovery of opioid analgesics with reduced side effects. *Nature* **537**, 185 (2016).
38. C. L. Schmid *et al.*, Bias factor and therapeutic window correlate to predict safer opioid analgesics. *Cell* **171**, 1165-1175. e1113 (2017).

39. B. Carpenter, R. Nehmé, T. Warne, A. G. W. Leslie, C. G. Tate, Structure of the adenosine A_{2A} receptor bound to an engineered G protein. *Nature* **536**, 104 (2016).
40. N. Saleh, G. Saladino, F. L. Gervasio, T. Clark, Investigating allosteric effects on the functional dynamics of β_2 -adrenergic ternary complexes with enhanced-sampling simulations. *Chem. Sci.* **8**, 4019-4026 (2017).
41. H. E. Kato *et al.*, Conformational transitions of a neurotensin receptor 1–G_{i1} complex. *Nature* **572**, 80-85 (2019).
42. M. Choi *et al.*, G protein–coupled receptor kinases (GRKs) orchestrate biased agonism at the β_2 -adrenergic receptor. *Sci. Signal.* **11**, eaar7084 (2018).
43. Y. Namkung *et al.*, Functional selectivity profiling of the angiotensin II type 1 receptor using pathway-wide BRET signaling sensors. *Sci. Signal.* **11**, eaat1631 (2018).
44. M. P. Jacobson, R. A. Friesner, Z. Xiang, B. Honig, On the role of the crystal environment in determining protein side-chain conformations. *J. Mol. Biol.* **320**, 597-608 (2002).
45. M. P. Jacobson *et al.*, A hierarchical approach to all - atom protein loop prediction. *Proteins Struct. Funct. Bioinform.* **55**, 351-367 (2004).
46. P. Ghanouni *et al.*, The Effect of pH on β_2 Adrenoceptor Function. *J. Biol. Chem.* **275**, 3121-3127 (2000).
47. A. Ranganathan, R. O. Dror, J. Carlsson, Insights into the role of Asp79^{2.50} in β_2 adrenergic receptor activation from molecular dynamics simulations. *Biochemistry* **53**, 7283-7296 (2014).
48. M. A. Lomize, A. L. Lomize, I. D. Pogozheva, H. I. Mosberg, OPM: orientations of proteins in membranes database. *Bioinformatics* **22**, 623-625 (2006).
49. R. Betz, Dabble (v2.6.3). Zenodo. <https://doi.org/10.5281/zenodo.836914>. (2017, August 1).
50. N. R. Latorraca *et al.*, Molecular mechanism of GPCR-mediated arrestin activation. *Nature* **557**, 452-456 (2018).
51. K. Fahmy *et al.*, Protonation states of membrane-embedded carboxylic acid groups in rhodopsin and metarhodopsin II: a Fourier-transform infrared spectroscopy study of site-directed mutants. *Proc. Natl. Acad. Sci. U.S.A.* **90**, 10206-10210 (1993).
52. M. Mahalingam, K. Martínez-Mayorga, M. F. Brown, R. Vogel, Two protonation switches control rhodopsin activation in membranes. *Proc. Natl. Acad. Sci. U.S.A.* **105**, 17795-17800 (2008).
53. C. W. Hopkins, S. Le Grand, R. C. Walker, A. E. Roitberg, Long-time-step molecular dynamics through hydrogen mass repartitioning. *J. Chem. Theory Comput.* **11**, 1864-1874 (2015).
54. J.-P. Ryckaert, G. Ciccotti, H. J. Berendsen, Numerical integration of the cartesian equations of motion of a system with constraints: molecular dynamics of n-alkanes. *J. Comp. Phys.* **23**, 327-341 (1977).

55. D. Beglov, B. Roux, Finite representation of an infinite bulk system: solvent boundary potential for computer simulations. *J. Chem. Phys.* **100**, 9050-9063 (1994).
56. J. Huang *et al.*, CHARMM36m: an improved force field for folded and intrinsically disordered proteins. *Nat. Methods* **14**, 71-73 (2016).
57. J. B. Klauda *et al.*, Update of the CHARMM all-atom additive force field for lipids: validation on six lipid types. *J. Phys. Chem. B* **114**, 7830-7843 (2010).
58. R. B. Best *et al.*, Optimization of the additive CHARMM all-atom protein force field targeting improved sampling of the backbone ϕ , ψ and side-chain χ_1 and χ_2 dihedral angles. *J. Chem. Theory Comput.* **8**, 3257-3273 (2012).
59. J. Huang, A. D. MacKerell Jr, CHARMM36 all - atom additive protein force field: Validation based on comparison to NMR data. *J. Comp. Chem.* **34**, 2135-2145 (2013).
60. D. A. Case *et al.*, *AMBER 2017* (University of California, San Francisco, 2017).
61. D. A. Pearlman *et al.*, AMBER, a package of computer programs for applying molecular mechanics, normal mode analysis, molecular dynamics and free energy calculations to simulate the structural and energetic properties of molecules. *Comput. Phys. Commun.* **91**, 1-41 (1995).
62. R. Salomon-Ferrer, A. W. Götz, D. Poole, S. Le Grand, R. C. Walker, Routine microsecond molecular dynamics simulations with AMBER on GPUs. 2. Explicit solvent particle mesh Ewald. *J. Chem. Theory Comput.* **9**, 3878-3888 (2013).
63. D. A. Case *et al.*, *AMBER 2018* (University of California, San Francisco, 2018).
64. D. A. Case *et al.*, *AMBER 2015* (University of California, San Francisco, 2015).
65. D. A. Case *et al.*, *AMBER 2016* (University of California, San Francisco, 2016).
66. K. Hukushima, K. Nemoto, Exchange Monte Carlo method and application to spin glass simulations. *J. Phys. Soc. Jpn.* **65**, 1604-1608 (1996).
67. A. Patriksson, D. van der Spoel, A temperature predictor for parallel tempering simulations. *Phys. Chem. Chem. Phys.* **10**, 2073-2077 (2008).
68. D. R. Roe, T. E. Cheatham III, PTRAJ and CPPTRAJ: software for processing and analysis of molecular dynamics trajectory data. *J. Chem. Theory Comput.* **9**, 3084-3095 (2013).
69. W. Humphrey, A. Dalke, K. Schulten, VMD: visual molecular dynamics. *J. Mol. Graph.* **14**, 33-38 (1996).
70. G. Pándy-Szekeres *et al.*, GPCRdb in 2018: adding GPCR structure models and ligands. *Nucleic Acids Res.* **46**, D440-D446 (2018).
71. D. P. Staus *et al.*, Sortase ligation enables homogeneous GPCR phosphorylation to reveal diversity in β -arrestin coupling. *Proc. Natl. Acad. Sci. U.S.A.* **115**, 3834-3839 (2018).

72. R. K. Türker, M. M. Hall, M. Yamamoto, C. S. Sweet, F. M. Bumpus, A New, Long-Lasting Competitive Inhibitor of Angiotensin. *Science* **177**, 1203-1205 (1972).
73. I. Domazet *et al.*, Characterization of Angiotensin II Molecular Determinants Involved in AT1 Receptor Functional Selectivity. *Mol. Pharmacol.* **87**, 982-995 (2015).
74. S.-I. Miura, S. S. Karnik, Angiotensin II type 1 and type 2 receptors bind angiotensin II through different types of epitope recognition. *J. Hypertens.* **17**, 397-404 (1999).